https://doi.org/10.1016/j.micromeso.2021.110944

Mechanical properties of colloidal calcium-silicate-hydrate gel with different gel-pore ionic solutions: a mesoscale study

Yohannes L. Yaphary,[a] Florence Sanchez,[b] Denvid Lau,[c] and Chi Sun Poon*[a]

[a] *Department of Civil and Environmental Engineering, The Hong Kong Polytechnic University, Hung Hom, Kowloon, Hong Kong*

[b]*Department of Civil and Environmental Engineering, Vanderbilt University, VU B 35 1831, Nashville, TN 37235, USA*

[c]*Department of Architecture and Civil Engineering, City University of Hong Kong, Hong Kong, China*

*Correspondence should be addressed to C.S. Poon (email address: cecspoon@polyu.edu.hk)

Abstract

The mechanical properties of hydrated cement paste are largely influenced by the interaction of nano-scale calcium-silicate-hydrate (C-S-H) particles that reside in the gel-pore aqueous ionic solution of colloidal C-S-H gel (C-S-H_{gel}). The ionic species and ionic concentration of the gel-pore solution can fluctuate – due to the hydration process of cement, the use of various admixtures, and ion exchange with the surrounding environment – and influence the dielectric constant (ε_r) of the gel-pore solution and the Debye length (κ^{-1}). Mesoscale simulations were employed to investigate the mechanical properties of C-S-H_{gel} with gel-pore ionic solutions of different ε_r and κ^{-1}. The results showed that ε_r and κ^{-1} influenced the packing density and cohesion of C-S-H_{gel}, and, in turn, its compressive stiffness, hardness, and strength. The lowest values of ε_r and κ^{-1} (i.e., highest ionic concentrations) resulted in higher stiffness, hardness, and strength. The information obtained in this study provided insight into the mechanism by which the gel-pore ionic solution affects the mechanical properties of C-S-H_{gel} and demonstrated that ε_r and κ^{-1} are useful parameters to consider when engineering design strategies for cementitious materials.

Keywords

Mesoscale simulations; Ionic solution; Electrical double layer; Calcium silicate hydrate (C-S-H), Mechanical properties

1. Introduction

The mechanical properties of hydrated cement paste (HCP) define its capability in transferring externally applied loads to resist structural failure of concrete. The HCP is a porous material with a pore ionic solution. The type and concentration of ions present in the pore solution can fluctuate due to the progress of cement hydration, the use of admixtures (i.e., mineral and chemical admixtures as well as salt containing constituents like seawater and sea sand) and the exposure to the surrounding environment, including exposure to solutions with different ionic concentrations. Such fluctuation in ionic species and concentration can differently affect the mechanical properties of the HCP [1, 2]. The HCP is a composite material that possesses a structural hierarchy comprised of different components at various scales [3]. The macroscale mechanical properties of the HCP is influenced by the mechanical properties of its components [4, 5]. Investigations on how different

ionic solutions affect the mechanical properties of the HCP components can provide a more fundamental and useful basis for the engineering of cementious material.

The different HCP components are formed during the dissolution-precipitation process of cement hydration. The dissolution process releases different ionic species that later precipitate (i.e., involving chemical reactions such as silica polymerization) upon reaching the saturation state and progressively turn into a solid structure [6]. The major end product of cement hydration at the equilibrium state is calcium-silicate-hydrate gel (C-S-H_{gel}) [7], which is believed to have a colloidal, particulate, and discrete nano-structure [8-10]. The colloidal C-S-H_{gel} has a low- (LD) and high-packing density (HD) and has different particle size distribution (PSD) and mechanical properties [11-13]. The C-S-H particles (C-S-$H_{particle}$) that comprise the C-S-H_{gel} are composed of C-S-H layers (C-S-H_{layer}) that have a structure similar to tobermorite and jennite [14]. The C-S-$H_{particle}$ are arranged and oriented (i.e., respecting their size and intrinsic C-S-H_{layer} direction) within the C-S-H_{gel} to achieve the equilibrium stage [15]. The mean Young's modulus of C-S-$H_{particle}$ can be obtained by Voigt-Reuss-Hill (VRH) average derived from anisotropic elasticity tensor C-S-H_{layer} [14]. Although the C-S-H_{layer} (i.e., a single C-S-$H_{particle}$) is anisotropic, the C-S-H_{gel} is isotropic [16]. Figure 1 shows a schematic representation of the C-S-H_{gel} nano-structure. It has been reported in the literature that the macroscale mechanical properties of the HCP largely originate from the interaction among the C-S-$H_{particle}$ [17, 18].

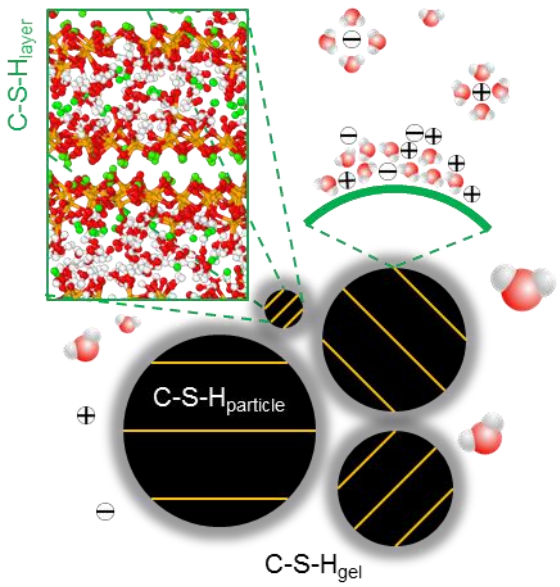

Figure 1. Schematic representation of the C-S-H_{gel} nano-structure adapted from [15], showing C-S-$H_{particle}$ in a gel-pore aqueous ionic solution. The C-S-$H_{particle}$ are composed of C-S-H_{layer} that have a structure similar to tobermorite and jennite [14].

Changes in ionic composition of the HCP gel pore solution has been found to affect the nano-structure of C-S-H_{gel}. Alite and cement pastes hydrated with NaOH [19] and seawater [20] have been reported to exhibit increased nanoindentation moduli. Furthermore, atomic force microscopy measurements have shown that the cohesion of the C-S-H_{gel} was influenced by the presence of ionic species and their concentration in the gel-pore solution [21]. Mesoscale simulations have indicated that the Debye length (κ^{-1}) of the electrolyte surrounding the C-S-$H_{particle}$ influenced their aggregation towards the C-S-H_{gel} formation [22]. However, a detailed understanding on how the characteristics of different ionic solutions affect the mechanical properties of C-S-H_{gel} and the interaction of the C-S-$H_{particle}$ is lacking. Yet, the presence of ionic species and their concentration in a colloidal system not only influence κ^{-1} but also the dielectric constant (ε_r) of the ionic solution [23]. Thus, knowledge of the effect of ε_r and κ^{-1} on the mechanical properties of C-S-H_{gel} can provide a mesoscale linkage between the characteristic of the gel-pore ionic solution of colloidal C-S-H_{gel} and the engineering performance of the cementitious material hydrated with different ionic solutions.

The present study aims to investigate the effect of the gel-pore ionic solution characterized in terms of ε_r and κ^{-1} on the mechanical properties of C-S-H_{gel} by using mesoscale simulations. The currently available information on the PSD of C-S-$H_{particle}$ was used to construct the models of LD and HD C-S-H_{gel}. The interactions of C-S-$H_{particle}$ were modeled with a pairwise potential, which considered ε_r and κ^{-1}. The investigated mechanical properties included compressive stiffness, hardness, and strength. The packing density and cohesion of C-S-H_{gel} were also investigated to reveal the effect of ε_r and κ^{-1} on C-S-H_{gel} structure that eventually affect the mechanical properties of C-S-H_{gel}. The results obtained not only provided insight into the ionic effect on the mechanical properties of C-S-H_{gel} but also demonstrated that ε_r and κ^{-1} are useful parameters for characterizing C-S-H_{gel} pore solutions that can improve the performance (e.g., mechanical properties and durability in aggressive environments) and sustainability (e.g., use of seawater and sea sand) of cementitious materials.

2. Mesoscale simulations

The mesoscale model consisted of C-S-$H_{particle}$ of different sizes in an implicit model of ionic solution and equilibrated as governed by the selected pairwise potential. The effect of the ionic solution on the mechanical properties of the C-S-H_{gel} was investigated by varying ε_r and κ^{-1}. Figure 2 shows the flowchart of the simulation stages.

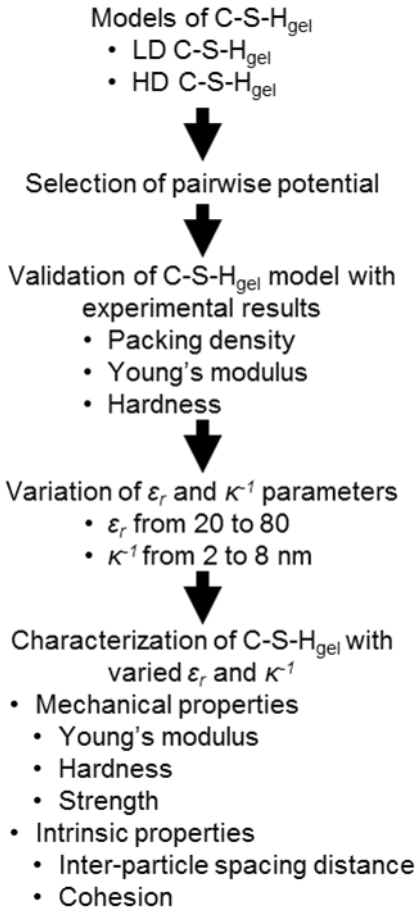

Figure 2. Flowchart of the simulation stages. LD and HD C-S-H_{gel} are low- and high-packing-density C-S-H_{gel}, respectively. ε_r and κ^{-1} are the dielectric constant and Debye length, respectively.

2.1 C-S-H_{gel} model

The C-S-H_{gel} was modeled as a polydisperse assembly of nano-scale colloidal (spherical) C-S-$H_{particle}$ (building blocks) that were surrounded by an ionic solution (i.e., implicitly characterized by ε_r and κ^{-1}). Based on information obtained from the literature [14, 15, 17, 24-26] on the characteristics of LD and HD C-S-H_{gel}, two models of C-S-H_{gel} with different PSD of spherical C-

S-$H_{particle}$ as shown in Figure 3 were studied. The spherical shape has been previously used to model C-S-$H_{particle}$ in mesoscale simulations of C-S-H_{gel} [27-29]. The model of LD C-S-H_{gel} consisted of C-S-$H_{particle}$ with a diameter of 5 nm, which is the size commonly used in the literature for monodisperse C-S-$H_{particle}$ to construct the LD C-S-H_{gel} model [28]. The HD C-S-H_{gel} was composed of C-S-$H_{particle}$ that followed a Gaussian PSD with a mean (μ) of 5 nm and a standard deviation (SD) of 8. These values provided a PSD ranging from 1-30 nm, which is the size-range of C-S-$H_{particle}$ typically reported in the literature from experiments [15, 17, 22, 25, 30]. Cubic simulation boxes with a length of 106 nm and containing 1,000 C-S-H particles were used to simulate the LD and HD C-S-H_{gel}. The number of C-S-$H_{particle}$ used was within the amount (i.e., a few hundred to several thousands) of particles typically used in the literature in previous studies [31-33]. In addition, a C-S-H_{gel} model with a simulation box of 228 nm in length and containing 10,000 C-S-$H_{particle}$ was used to verify that the C-S-H_{gel} model with 1,000 C-S-$H_{particle}$ was sufficient to represent a large simulation system.

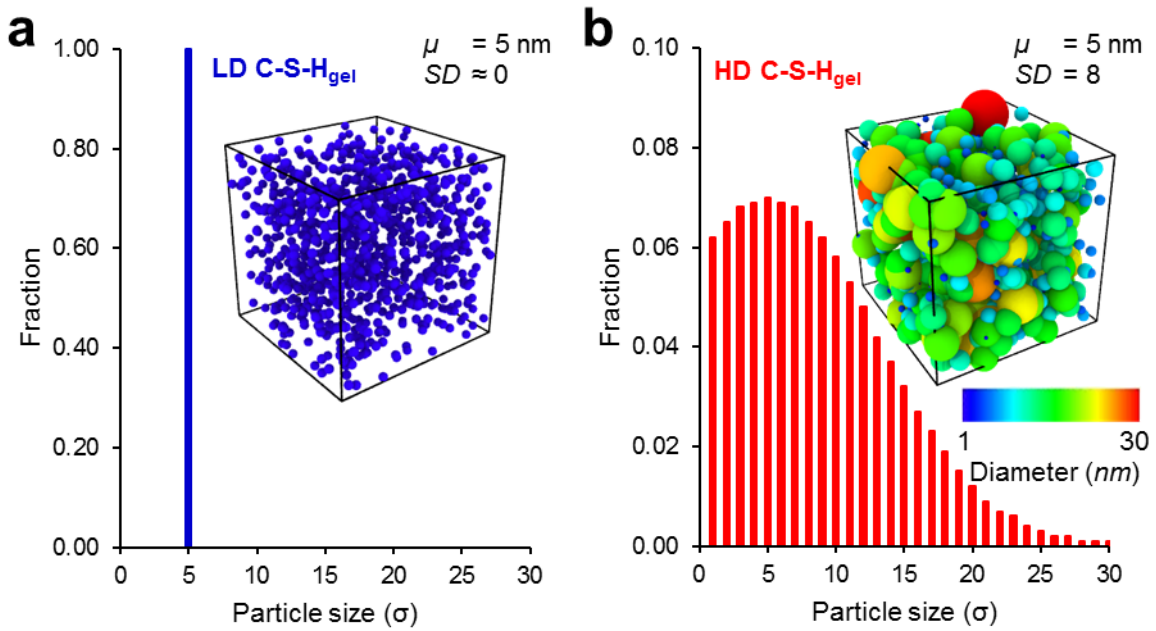

Figure 3. Particle size distribution (PSD) of (a) low- (LD) and (b) high-packing-density (HD) C-S-H_{gel}. Gaussian distribution was assumed for the HD C-S-H_{gel} with μ and *SD* as mean and standard deviation, respectively. The LJ unit of σ is equal to the physical unit of nm.

A schematic representation of the interface between the surface of a C-S-$H_{particle}$ and the gel-pore ionic solution of the C-S-H_{gel} showing the electrical double layer (EDL) at the surface of the C-S-$H_{particle}$ and the ions in the gel-pore solution is given in Figure 4. The EDL of the C-S-$H_{particle}$ is initiated by the surface formation of the silanol sites (i.e., negatively surface charge) during the hydration of cement [34]. In the high pH environment of the pore solution of C-S-H_{gel}, Ca^{2+} cations are adsorbed by the silanol sites [35] and act to decrease the potential surface charge of C-S-$H_{particle}$ [36]. The lower potential surface charge is associated with the initial agglomeration of C-S-$H_{particle}$ to form cohesive C-S-H_{gel}. Similar to other colloidal systems, the ionic solution of the cohesive C-S-H_{gel} can be characterized by ε_r and κ^{-1}.

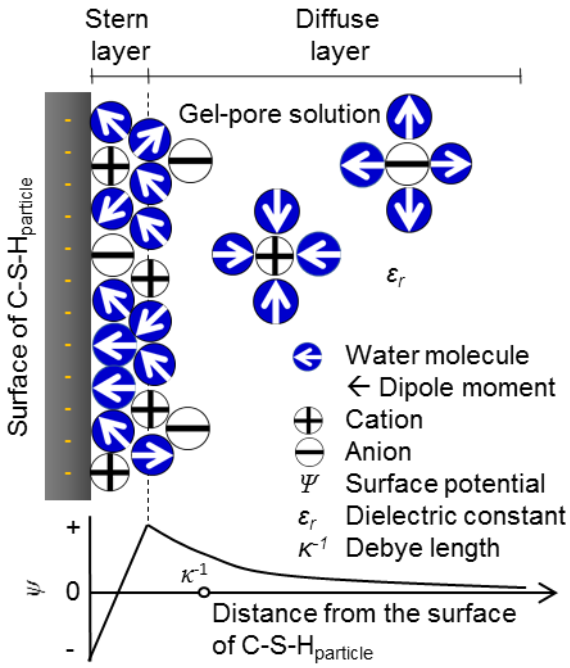

Figure 4. Schematic representation of the interface between the surface of C-S-$H_{particle}$ and the gel-pore ionic solution. Adapted from [37].

2.2 C-S-$H_{particle}$ interactions

The combined pairwise potential for C-S-$H_{particle}$ interactions was used. This potential considers ε_r and κ^{-1} to estimate the C-S-$H_{particle}$ interactions (Equation 1). The first term in Equation 1 is the Lennard-Jones (LJ) pairwise potential, which has been commonly used in the literature to estimate

the attractive profile of C-S-$H_{particle}$ [22, 28, 31]. The second term is the hard-core pairwise repulsive Yukawa potential that considers ε_r and κ^{-1} [38, 39].

$$V = 4\varepsilon\left(\left(\frac{\sigma_{ij}}{r}\right)^{2\gamma} - \left(\frac{\sigma_{ij}}{r}\right)^{\gamma}\right) + \frac{C_{VR}}{\kappa} exp^{-\kappa(r-\sigma_{ij})} \quad (1)$$

In the first term of Equation 1, ε is the depth of the potential well (Equation 2) [27, 28], σ_{ij} is the averaged diameter of particles i (diameter σ_i) and j (diameter σ_j) as expressed in Equation 3, r is the centre-to-centre distance of particles i and j, γ is the LJ exponent, k is a constant determined from the serial spring model of C-S-H_{gel} (k = 0.002324) [40, 41], and E is the Young's modulus (E = 63.6 GPa from atomistic simulations of C-S-H_{layer} [40, 41]). For γ, a value of 14 was selected to obtain a rupture strain (ε_u) of 4.8% as per Equation 4, which was in good agreement with the estimation of 5% from the atomistic simulation results reported in [14].

$$\varepsilon = kE\sigma_i\sigma_j\sigma_{ij} \quad (2)$$

$$\sigma_{ij} = \frac{\sigma_i+\sigma_j}{2} \quad (3)$$

$$\varepsilon_u = \frac{\left(\sqrt[\gamma]{\frac{4\gamma+2}{\gamma+1}}\sigma_{ij} - \sqrt[\gamma]{2}\sigma_{ij}\right)}{\sqrt[\gamma]{2}\sigma_{ij}} \quad (4)$$

In the second term of Equation 1, κ^{-1} is the Debye length and C_{VR} is the repulsive potential energy at the surface of C-S-$H_{particle}$ [36]. In the framework of coarse-grained simulation, the value of C_{VR} can be adjusted to fit the profile of pairwise potential. A κ^{-1} value of 5 nm and C_{VR} value of 0.003 $k_BT.\varepsilon^{-1}$ were selected, so that a similar profile of pairwise potential and force of C-S-$H_{particle}$ interactions to that developed by Ioannidou et al. [22] was obtained. Profiles of the pairwise potential and force are shown in Figure 5. The pairwise force is the derivative of pairwise potential with respect to the inter-particle distance. The pairwise potential and force were defined by the Lennard-Jones and hard-core Yukawa's pairwise potential over the inter-particle distance (Equation 1).

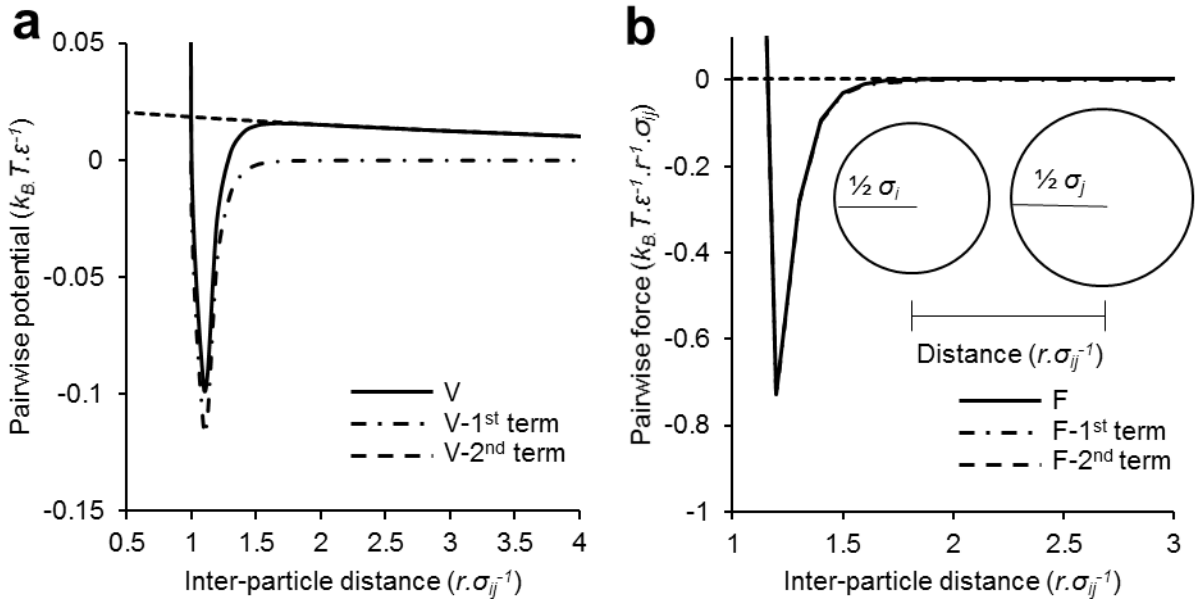

Figure 5. (a) Pairwise potential and (b) pairwise force as a function of inter-particle distance. V-1st term (F-1st term), V-2nd term (F-2nd term) and V (F) are the attractive (negative values), repulsive (i.e., positive values), and total pairwise potential (pairwise forces), respectively.

To study the effect of the gel-pore ionic solution, the value of ε_r was varied from 20 to 80 in increments of 10 for fixed values of κ^{-1} corresponding to 2, 5 and 8 nm. The values of ε_r and κ^{-1} were chosen to be below and above those of a reference C-S-H_{gel} for which ε_r and κ^{-1} were assumed to be 30 and 5 nm, respectively. ε_r values ranging from 16-40 [42] and value of κ^{-1} varying by a few nm [22, 36, 43] have been reported in the literature for HCP. The upper ε_r value of 80 corresponded to that of water [44]. Changes in ε_r affected the C_{VR} value with respect to that of the reference C-S-H_{gel} (0.003 $k_BT.\varepsilon^{-1}$ for C_{VR-ref}) according to equation 5 [39]. The selected range of ε_r corresponded to C_{VR} values ranging from 0.002 to 0.008 $k_BT.\varepsilon^{-1}$.

$$C_{VR} = \frac{\varepsilon_r}{\varepsilon_{r-ref}} C_{VR-ref} \quad (5)$$

2.3 Mechanical properties

The mesoscale simulations were performed using LAMMPS (Large-scale Atomic/Molecular Massively Parallel Simulator), which is a well-tested and widely used open source code for simulations at varying length and time scales [45]. Periodic boundary conditions were applied in

all directions throughout the simulation stage. In order to investigate the mechanical properties, the C-S-H_{gel} was first equilibrated under NPT ensemble at a temperature of 300 K and a pressure of 0 GPa. The averaged potential energy and root-mean-square displacement (RMSD) of the C-S-$H_{particle}$ were monitored as a function of time until a steady state was achieved to ensure equilibrium. The RMSD at the equilibrium state was chosen to correspond to the vibration of C-S-$H_{particle}$ within 0.05 nm. Following the equilibration process of LD and HD C-S-H_{gel}, the mechanical properties were investigated as a function of ε_r and κ^{-1}.

The compressive stiffness and strength were determined (i.e., after equilibration state) under uniaxial deformation in one direction. While performing the deformation, the pressure along the other two directions was maintained at 0 GPa. The strain rate was 0.005 for each deformation, which was performed with a timestep of 0.0001 τ (i.e., LJ unit for time). The strain rate and timestep were selected to attain a pressure of 0 GPa along the two lateral directions for a stable simulation during the uniaxial deformation. The non-pressure setting in the directions perpendicular to the deformation was used to eliminate the artificial constrain and allow the free development of compression without any restriction [46]. The gradually evolved pressure along the deforming direction was plotted against the strain to obtain the stress-strain profile. Based on this profile, the compressive Young's modulus and ultimate strength were determined. The Young's modulus (E_c) was calculated from the slope of the stress-strain curves [47]. The best linear fit was determined from the group of stress-strain data with a strain increment of 0.001 (i.e., within the linear portion of the stress-strain plot) that had an optimum R^2. The ultimate strength ($f_{c\text{-}u}$) was determined as the maxima of the stress-strain profile.

The hardness of the C-S-H_{gel} (H_c) was determined based on the determination of the Mohr-Coulomb failure envelope, which is a function of the normal and shear stress [48-50], and was approximated as 5.8 times that of the cohesive stress, C [48]. The C was obtained from the intercept with the axis of the failure envelope of the shear stress. The Mohr-Coulomb failure envelope was determined by performing the uniaxial compressive deformation under three different lateral pressures (i.e., 0.00, 0.05 and 0.10 GPa). The maximum elastic compressive strengths ($f_{c\text{-}e}$) were then obtained from the developed stress-strain profiles under the three different lateral pressures. By adopting the similar identification of the elastic limit or yield stress from the macroscale stress-strain profile, the $f_{c\text{-}e}$ is determined as the average of the first local maximum and minimum stresses before the strain hardening curve. Afterward, the lateral pressures and $f_{c\text{-}e}$ from the three cases of

different lateral pressures were used to draw the Mohr circles. The envelope of the Mohr circles was fitted by a Mohr-Coulomb failure criterion (Equation 6).

$$\tau_c = C - f_{c-e} tan\theta \quad (6)$$

Where τ_c, C, $f_{c\text{-}e}$ and θ are the shear stress, cohesive stress, maximum elastic compressive stress, and friction angle, respectively.

2.4 Inter-particle spacing distance and cohesion of C-S-H_{gel}

To better understand the effect of ε_r and κ^{-1} on the mechanical properties of LD and HD C-S-H_{gel}, the inter-particle spacing distance and cohesion of C-S-H_{gel} were investigated. The inter-particle spacing distance was approximated by considering the Voronoi volume (V_v) of the particles as spheres. The inter-particle spacing distance (d_B) was then calculated by using Equation 7.

$$d_B = 2\left(\frac{3}{4\pi} V_v\right)^{1/3} \quad (7)$$

Steered molecular dynamics (SMD) simulations were employed to examine the cohesive energy of the C-S-H_{gel}. SMD applies a steered external force to accelerate the conformational change of the investigated system along the assumed path [51]. Thus, the process can be observed within the time scale that is applicable to MD. By employing the Jarzynski's equality in the framework of SMD, the potential of mean force (PMF) can be used to capture the energy of the system studied [52]. SMD is a simulation method that allows to study force-induced behaviour and probe the molecular mechanisms of the binding forces between particles, similar to atomic force microscopy experiments. The configuration used for the SMD simulations along with the parameters is shown in Figure 6. After the equilibration process under the NPT ensemble, the simulation box was enlarged three times from the equilibrated size in the direction of pulling by SMD simulations. Subsequently, the C-S-H_{gel} was equilibrated under NVT ensemble at a temperature of 300 K. Then, the lower one third of the bottom part of the C-S-H_{gel} was restrained and the upper third part was vertically pulled. The conformational change of the pulling virtual spring (i.e., along with its stiffness value of k) facilitated the calculation of the cohesive energy.

The cohesive energy was associated with the potential mean force (PMF) [52]. The obtained cohesive energy to separate the upper part of C-S-H_{gel} from its lower part was then normalized to 1 nm^2. The spring was assigned with a stiffness (k) of 1000 GPa.nm and was pulled with three different speed (v) of 1, 0.1 and 0.01 $nm.\tau^{-1}$.

The LJ unit was employed for the time dimension to allow the qualitative comparison of the cohesion of the LD and HD C-S-H_{gel} under different ε_r and κ^{-1} by using SMD. The experimentally obtained LD and HD C-S-H_{gel} cohesions remain missing to scale the LJ's time unit to the real one. However, the AFM experiment has been performed to show the role of ionic presence on the cohesion of HCP [21]. The information from AFM experiment can be used to qualitatively validate the finding from our simulation to demonstrate the ionic role on the cohesion of C-S-H_{gel}.

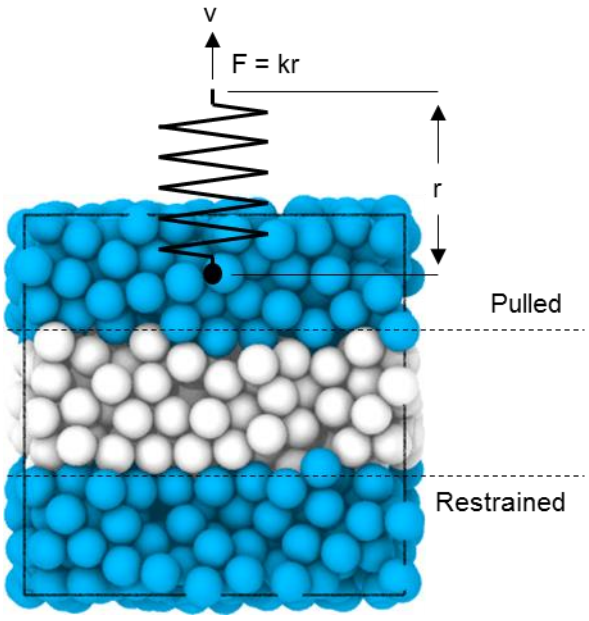

Figure 6. Schematic representation of the configuration used for the steered molecular dynamics (SMD) simulations of the C-S-H_{gel}. The lower one-third part of the C-S-H_{gel} was restrained. The virtual spring of SMD was tethered at the centre of the upper third part of the C-S-H_{gel}.

3. Result and discussion

3.1 Validation of the mesoscale model

The reference C-S-H_{gel} (ε_r = 30 and κ^{-1} = 5 nm) was used to validate the mesoscale model prior to the study of the effect of different gel-pore ionic solutions on the packing density (η) and mechanical properties of C-S-H_{gel}. The size of the simulation box (106 nm versus 228 nm) and number of C-S-$H_{particle}$ (1,000 versus 10,000) in the simulation box were evaluated. The greater η of the reference HD C-S-H_{gel} compared to the reference LD C-S-H_{gel} (Figure 7) was associated with the interspacing occupation of the large C-S-$H_{particle}$ with small C-S-$H_{particle}$. Consistent with the η, the mechanical properties (ultimate compressive strength $f_{c\text{-}u}$, Young's modulus E_c, and hardness H_c) of the reference LD C-S-H_{gel} were lower than those of the reference HD C-S-H_{gel} (Figure 8). The simulation results for the η, E_c, and H_c of the reference LD and HD C-S-H_{gel} overall compared well with experimental results of nanoindentation reported in the literature [16] as summarized in Table 1. In addition, there was no significant difference in the simulation results when 10,000 C-S-$H_{particle}$ were used in the simulation box compared to when 1,000 C-S-$H_{particle}$ were used. A simulation box with 1,000 C-S-$H_{particle}$ was thus used for the remainder of the study.

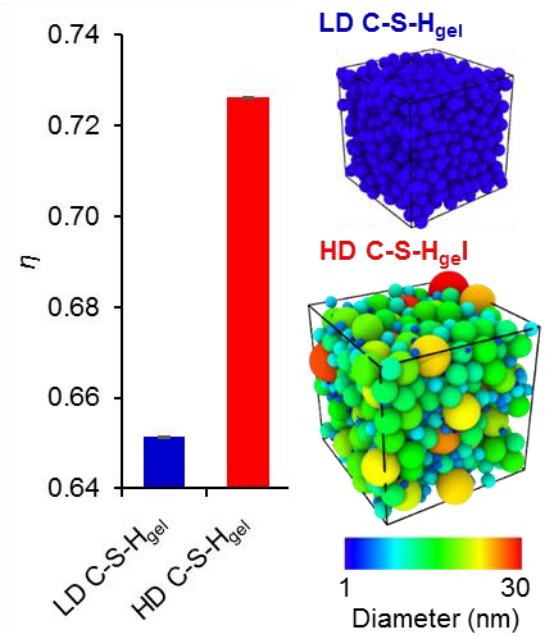

Figure 7. Packing density (η) of LD and HD C-S-H_{gel} by volume (1,000 C-S-$H_{particle}$) after equilibration state in NPT ensemble with temperature of 1 300 K and pressure of 0 GPa. The size of the simulation boxes of LD and HD C-S-H_{gel} after equilibration was 46.489^3 nm^3 and 106.170^3 nm^3, respectively.

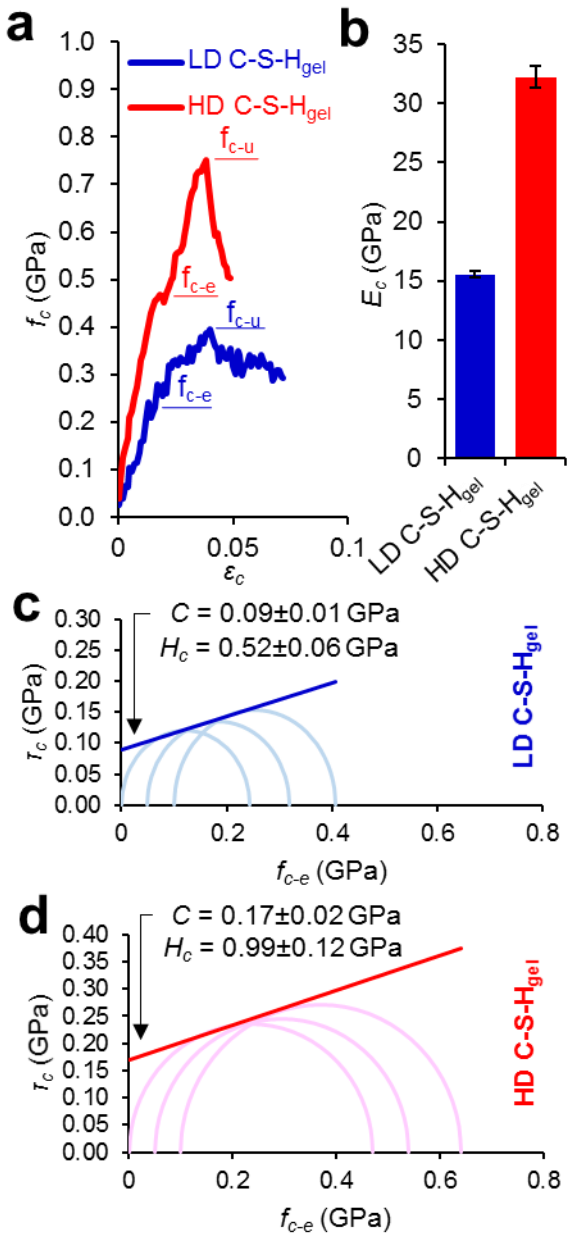

Figure 8. (a) Stress-strain profile, (b) Young's modulus (E_c) and (c) and (d) Mohr-Coulomb and Hardness (H_c) of LD and HD C-S-H_{gel}. f_c is the compressive stress. The ultimate compressive strength ($f_{c\text{-}u}$) of LD and HD C-S-H_{gel} was 0.40±0.05 GPa and 0.75±0.06 GPa, respectively. τ_c is the shear stress from the envelope of the Mohr's circles that was fitted by a Mohr-Coulomb failure criterion.

Table 1. Comparison of simulation results obtained for two different numbers of C-S-$H_{particle}$ (1,000 and 10,000) in the C-S-H_{gel} model with nanoindentation results from the literature [16] for the packing density (η), Young's modulus (E_c), and hardness (H_c) of low- (LD) and high-packing-density (HD) C-S-H_{gel}.

Property	Number of C-S-$H_{particle}$	LD		HD	
		Simulation	Experiment [16]	Simulation	Experiment [16]
η	1,000	$0.651\pm2.2\times10^{-5}$	0.647±0.048	$0.726\pm0.1\times10^{-5}$	0.746±0.047
η	10,000	$0.653\pm4.7\times10^{-5}$		$0.727\pm0.6\times10^{-5}$	
E_c (GPa)	1,000	15.52±0.27	18.69±4.75	32.24±0.92	32.10±5.23
E_c (GPa)	10,000	15.71±0.28		32.78±0.57	
H_c (GPa)	1,000	0.52±0.06	0.46±0.19	0.99±0.12	0.97±0.24
H_c (GPa)	10,000	0.59±0.02		0.87±0.08	

The values of the simulated $f_{c\text{-}u}$ of the reference LD and HD C-S-H_{gel} were between the values found in the literature for the C-S-H_{layer} (several GPa [47]) and HCP (0.07 to 0.8 GPa for water-to-cement ratios ranging from 0.075 to 0.4 [53]). The decreasing trend of $f_{c\text{-}u}$ from C-S-H_{layer} to C-S-H_{gel} and HCP as shown in Figure 9 was consistent with their increasing porosity. C-S-H_{layer} is composed of atomic structure and has no porosity (i.e., the interatomic space within the C-S-H_{layer} is not considered as effective porosity). The porosity of C-S-H_{gel} consists of the gel-pore and that of HCP is composed of the sum of the gel and capillary pores.

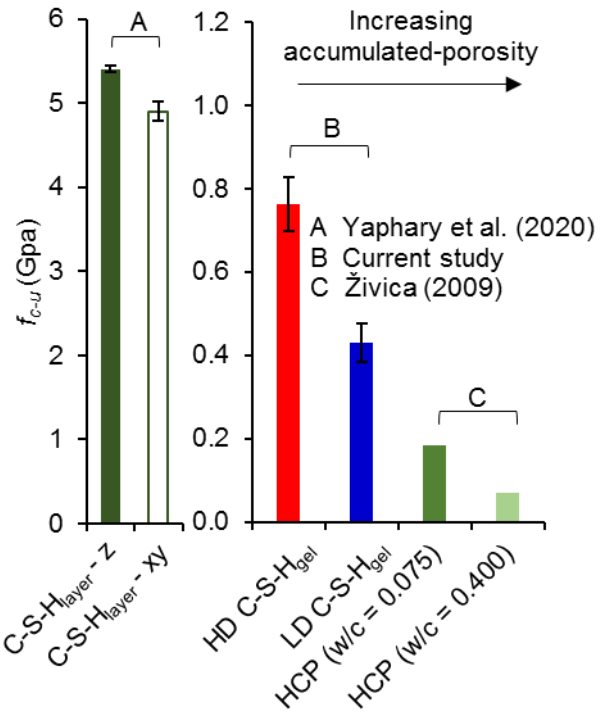

Figure 9. $f_{c\text{-}u}$ of hydrated cement paste (HCP) and its components. Results from this paper shown for comparison. The $f_{c\text{-}u}$ of C-S-H_{layer}-z and -xy are the values measured along the parallel and perpendicular directions to the layer of C-S-H_{layer}, respectively.

3.2 Effect of dielectric constant (ε_r) and Debye length (κ^{-1}) on packing density (η) of C-S-H_{gel}

For both the LD and HD C-S-H_{gel}, a decrease in ε_r and κ^{-1} (i.e., increase in ionic concentration) resulted in an increase in η (Figure 10). This result was consistent with a greater inter-C-S-$H_{particle}$ attraction for lower values of ε_r and κ^{-1} (greater ionic concentration) and was in good agreement with a greater cohesion of C-S-H_{gel} reported in the literature in the presence of salt-based admixtures such as $CaCl_2$ [54-56]. The effect of ε_r and κ^{-1} was more noticeable for the LD C-S-H_{gel} than the HD C-S-H_{gel}. This was thought to be attributed to the greater pore space filled by the gel-pore ionic solution between C-S-$H_{particle}$ for the LD C-S-H_{gel} compared to the HD C-S-H_{gel}.

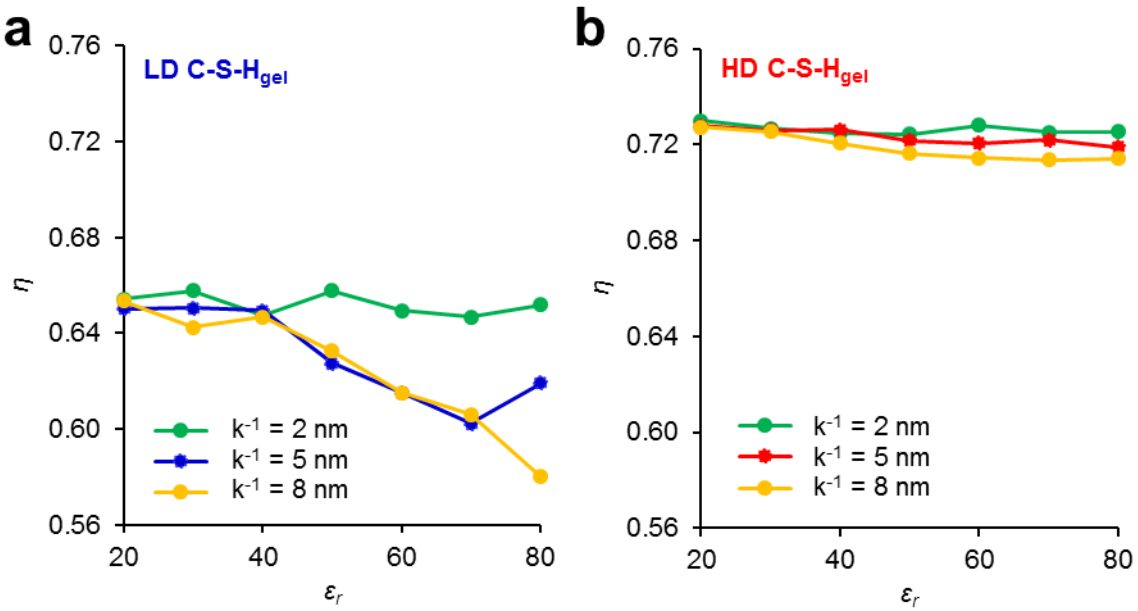

Figure 10. η of (a) LD C-S-H$_{gel}$ and (b) HD C-S-H$_{gel}$ as a function of the dielectric constant (ε_r) for different values of the Debye length (κ^{-1} = 2, 5, and 8 nm). Standard deviations were small and therefore not visible.

3.3 Effect of ε_r and κ^{-1} on the mechanical properties of C-S-H$_{gel}$

The effect of ε_r and κ^{-1} on the mechanical properties of the C-S-H$_{gel}$ is shown in Figures 11, 12, and 13. Overall, there was a tendency for the lower values of ε_r and κ^{-1} (greater ionic concentration) to result in higher E_c, H_c and $f_{c\text{-}u}$. The intensified tendency depends on the difference between the two paired ε_r and κ^{-1} selected to observe the changing effect of ε_r and κ^{-1} on E_c, H_c, *and* $f_{c\text{-}u}$. The higher the difference between two paired ε_r and κ^{-1} is, the higher the probability of observing the apparent contrast of E_c, H_c, *and* $f_{c\text{-}u}$ is. The t-test was performed to confirm the tendency for resulting in higher E_c, H_c and $f_{c\text{-}u}$ from lowering the values of ε_r and κ^{-1}. The t-test indicated that the probability of obtaining higher E_c, H_c, *and* $f_{c\text{-}u}$ values by decreasing ε_r and κ^{-1} was above 95% for both the LD and HD C-S-H$_{gel}$. The greater likelihood of higher E_c, H_c, and $f_{c\text{-}u}$ values with decreasing ε_r and κ^{-1} is further shown in Figure 14 as obtained from 21 combinations of ε_{ri} and ε_{rj} (i.e., $\varepsilon_{ri} > \varepsilon_{rj}$) for a fixed value of κ^{-1} and 3 combinations of ${\kappa^{-1}}_i$ and ${\kappa^{-1}}_j$ (i.e., ${\kappa^{-1}}_i > {\kappa^{-1}}_j$) for a fixed value of ε_r.

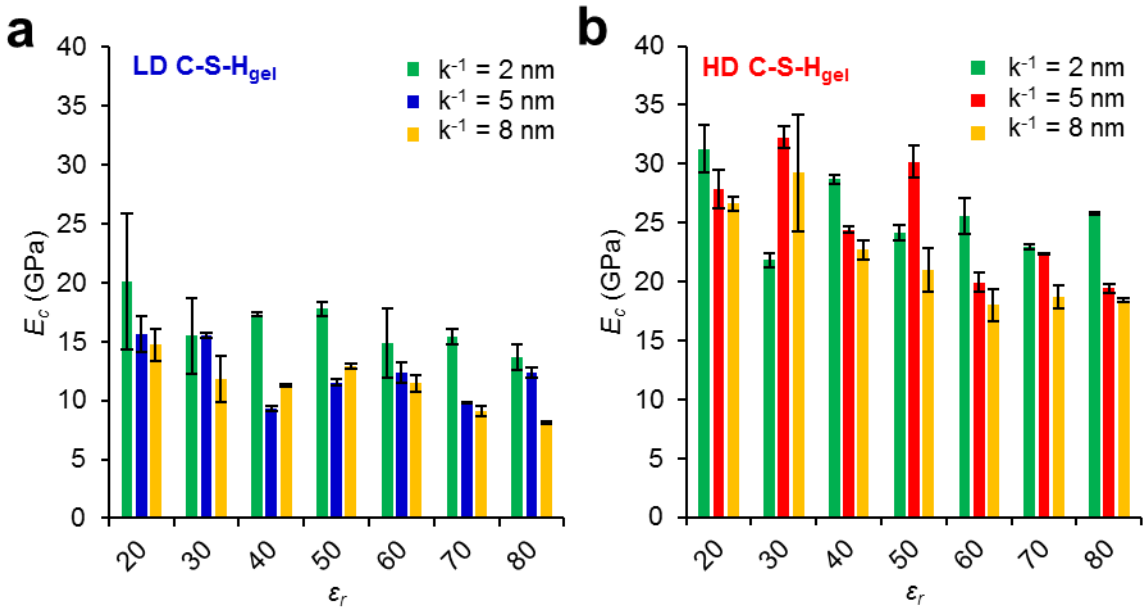

342

343 Figure 11. E_c for different ε_r and κ^{-1} for (a) LD C-S-H$_{gel}$ and (b) HD C-S-H$_{gel}$.

344

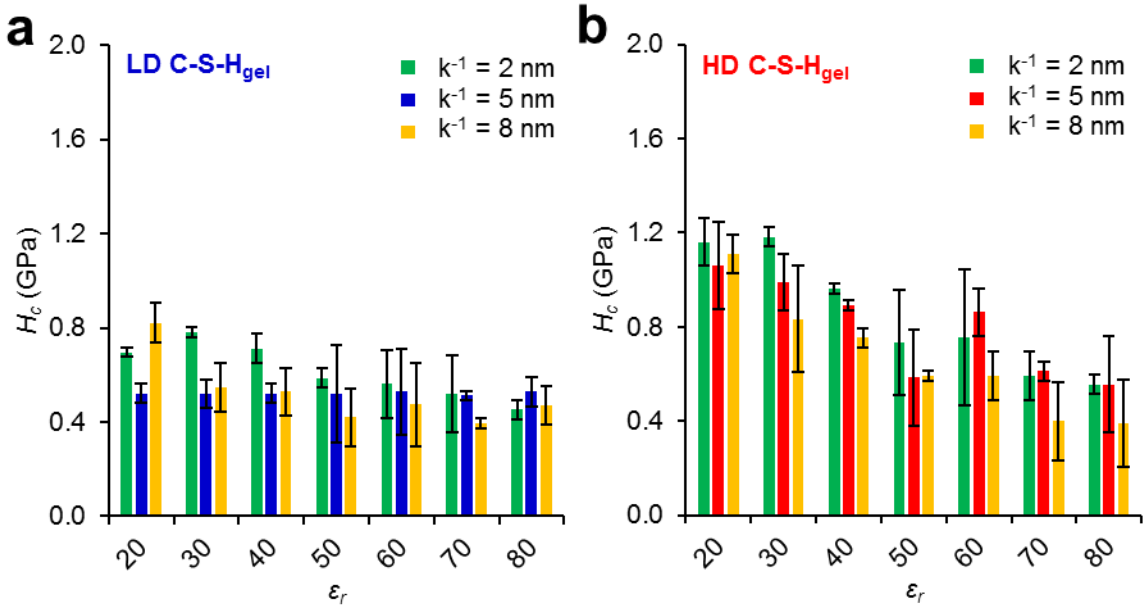

345

346 Figure 12. H_c for different ε_r and κ^{-1} for (a) LD C-S-H$_{gel}$ and (b) HD C-S-H$_{gel}$.

347

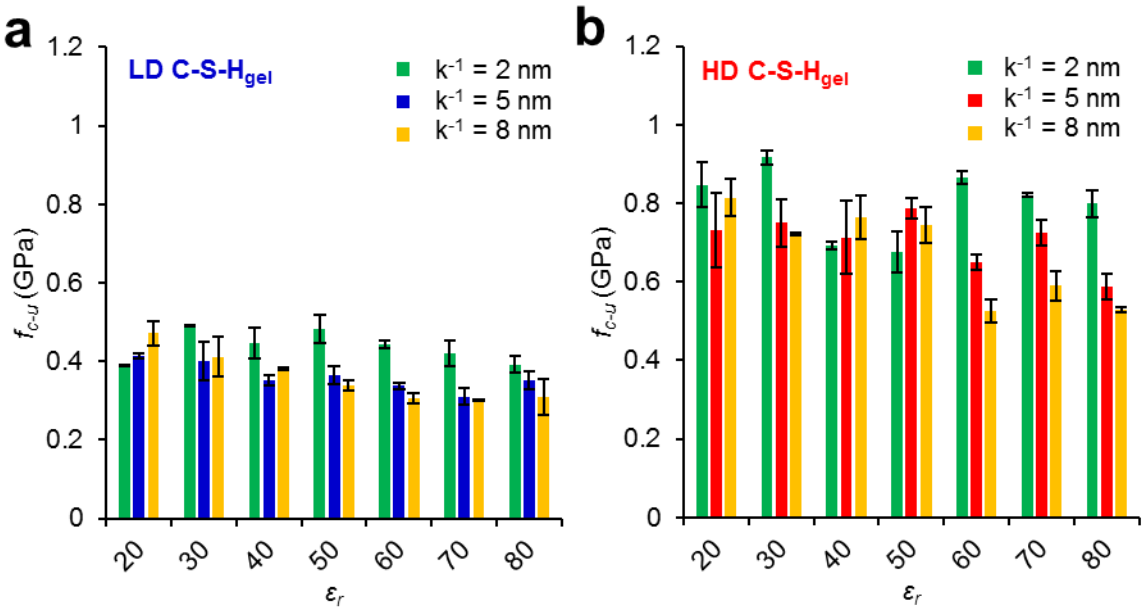

Figure 13. $f_{c\text{-}u}$ for different ε_r and κ^{-1} for (a) LD C-S-H$_{gel}$ and (b) HD C-S-H$_{gel}$.

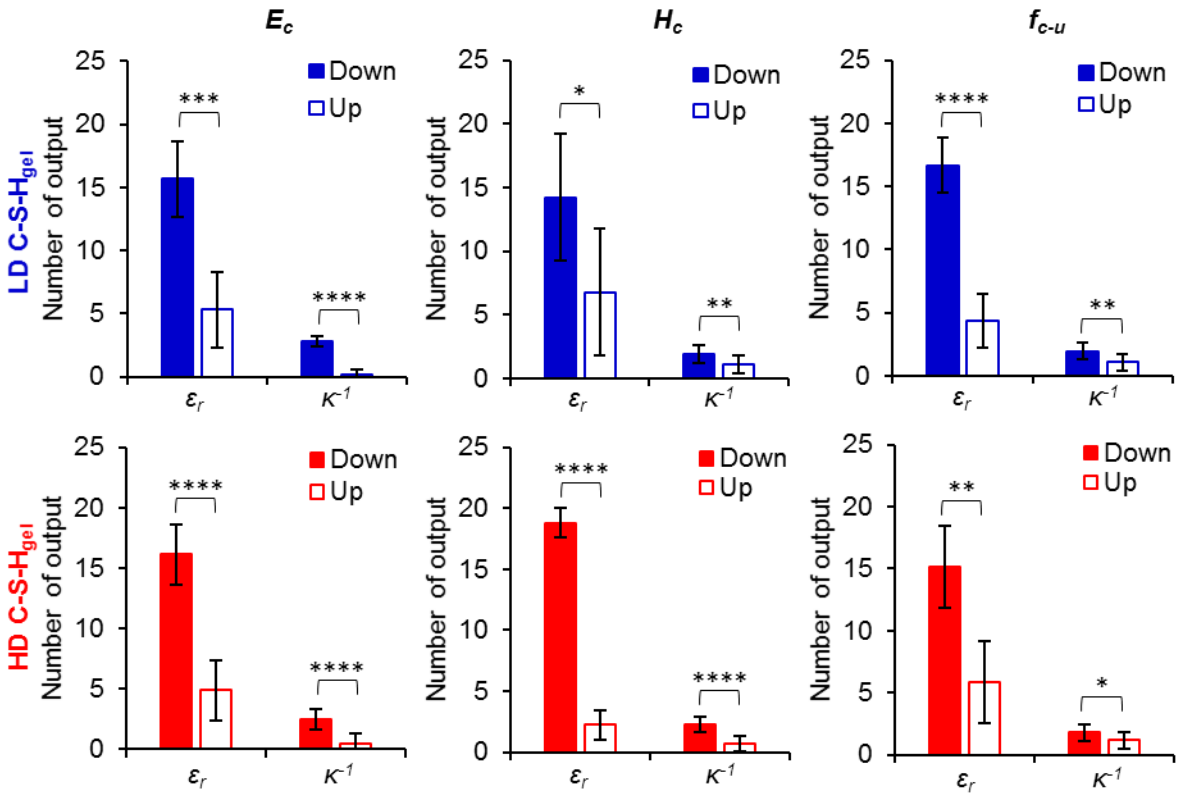

Figure 14. Comparison of the number of output that resulted in increasing (up, open bars) and decreasing (down, closed bars) effect on E_c, H_c *and* f_{c-u} values by lowering the values of ε_r and κ^{-1}.

These results were consistent with the higher nanoindentation modulus results reported for hydrated alite and cement prepared with the addition of NaOH [19] and seawater [20], respectively that were attributed to the formation of a denser C-S-H_{gel}. The presence of ions in the interstitial solution of hydrating alite or cement provides for greater ionic adsorption onto the surface of the C-S-$H_{particle}$ and thus cohesion of the HCP [19]. The effect of a greater ionic adsorption is a dielectric decrement, that is, a reduction of ε_r of the solution. The adsorbed ions furthermore provide a screening of the surface charge of the C-S-$H_{particle}$, thus reducing κ^{-1} [24, 34, 35]. The mesoscale simulation results demonstrated that a decrease in ε_r and κ^{-1}, and thus increase in ionic concentration of the gel-pore solution similar to that with the addition of NaOH or seawater, resulted in an increase in η and E_c. These results further confirmed that ε_r and κ^{-1} are suitable parameters that can be used to link the presence of ions to the effect on the mechanical properties of C-S-H_{gel}.

3.4 Plot of mechanical properties versus packing density of C-S-H_{gel}

In order to examine the correlation between the physical change and mechanical properties of C-S-H_{gel}, the mechanical properties versus packing density (i.e., η-E_c, η-H_c and η-$f_{c\text{-}u}$ plots) for the LD and HD C-S-H_{gel} were plotted as shown in Figure 15. There was a clear tendency for E_c, H_c and $f_{c\text{-}u}$ to increase with η. This positive correlation was in good agreement with results from previous studies reported in the literature [16, 31, 40, 57]. A much greater effect of η was seen on the mechanical properties of the HD C-S-H_{gel} than of the LD C-S-H_{gel}. This was in contrast with the effects of ε_r and κ^{-1} that were greater for the η of the LD C-S-H_{gel} than of the HD C-S-H_{gel}. This was thought to be associated with the effect of ε_r and κ^{-1} on the physical characteristics of the C-S-$H_{particle}$ and the factors defining the mechanical strength of C-S-H_{gel} (i.e., inter-C-S-$H_{particle}$ spacing distance and cohesive energy of C-S-H_{gel}).

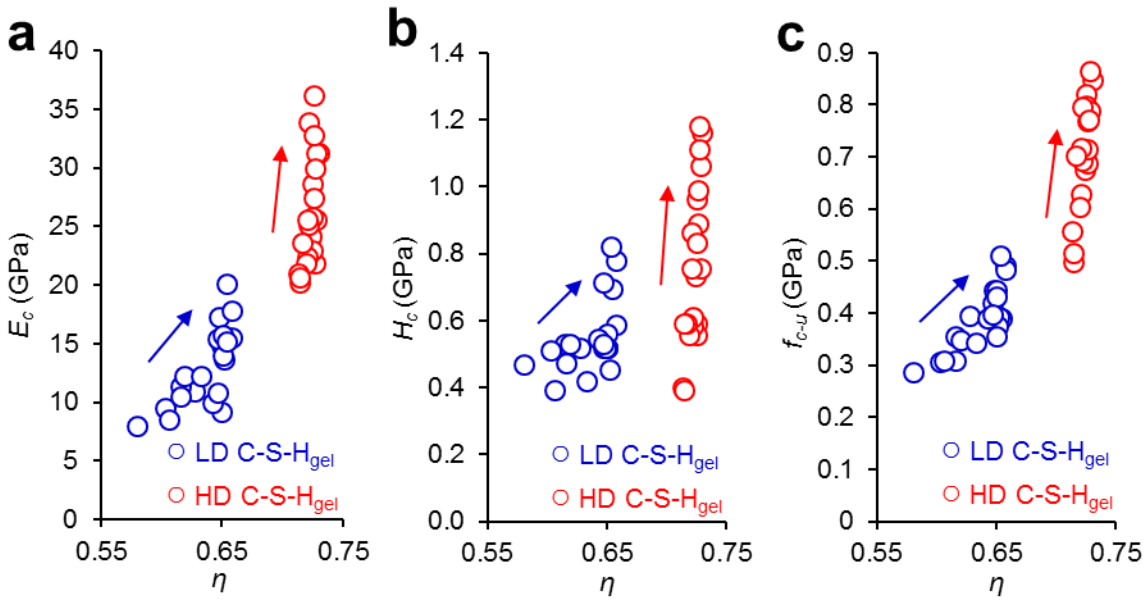

Figure 15. Scatter plots of (a) packing density-Young's modulus (η-E_c), (b) packing density-hardness (η-H_c), and (c) packing density-ultimate compressive strength (η-$f_{c\text{-}u}$) of LD and HD C-S-H_{gel}.

3.5 Inter-C-S-$H_{particle}$ spacing distance and cohesion of C-S-H_{gel}

The effect of ε_r and κ^{-1} on the inter-C-S-$H_{particle}$ spacing distance and cohesive energy of C-S-H_{gel} was investigated using the lowest (i.e., ε_r = 20 and k^{-1} = 2 nm) and highest (80 and k^{-1} = 8 nm)

paired values of the ε_r and κ^{-1} range examined. The difference in inter-C-S-$H_{particle}$ spacing distance between the low and high-paired values of ε_r and κ^{-1} was more significant for the LD C-S-H_{gel} than the HD C-S-H_{gel} (Figure 16). This result was consistent with the greater effect of ε_r and κ^{-1} seen on the η of the LD C-S-H_{gel}.

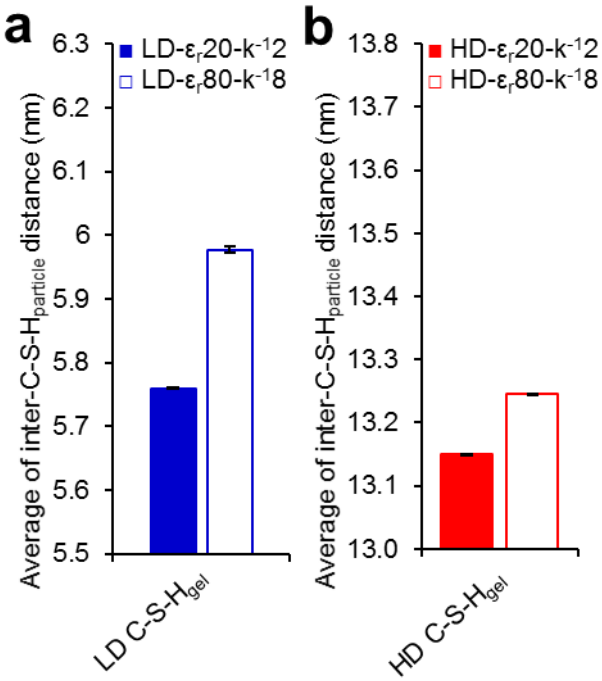

Figure 16. Average inter-C-S-$H_{particle}$ spacing distance of (a) LD C-S-H_{gel} and (b) HD C-S-H_{gel} with low (ε_r20-k^{-1}2, corresponding to ε_r = 20 and k^{-1} = 2 nm) and high (ε_r80-k^{-1}8, corresponding to ε_r = 80 and k^{-1} = 8 nm) paired values of ε_r and κ^{-1}.

Figure 17 shows the potential mean force (PMF) profile obtained from steered molecular dynamics (SMD) simulations. The PMF is a one-dimensional free energy landscape of C-S-$H_{particle}$ interactions and can be used to indicate the change in cohesion of C-S-H_{gel} due to different ε_r and κ^{-1}. The effect of the pulling speed on the PMF profile was relatively minimal at low speed values (i.e., from 0.1 to 0.01 nm.τ^{-1}). Regardless of the pulling speed (i.e., 1 and 0.01 nm.τ^{-1}), the effect of changing ε_r and κ^{-1} on the ultimate PMF was more significant on the HD C-S-H_{gel} than the LD C-S-H_{gel} (Figure 18). This was consistent with the more significant effect of η on E_c, H_c, and $f_{c\text{-}u}$ of the HD C-S-H_{gel} than LD C-S-H_{gel} even though the effect of ε_r and κ^{-1} on η of the former was less significant than that of the latter. The change in ε_r and κ^{-1} was demonstrated to influence the

inter-C-S-$H_{particle}$ spacing distance and η and, in turn, to lead to changes in cohesion and mechanical properties of the C-S-H_{gel}. Figure 18 also shows that the cohesion of C-S-H_{gel} increases from the system with higher to lower ε_r and κ^{-1}. This observation is consistent with the finding from AFM experiment that showed the generated cohesion of HCP in the ionic presence [21]. The HCP cohesion was attributed to the ionic pore solution (i.e., lower ε_r due to dielectric decrement [58, 59]) and the lower potential surface charge of C-S-$H_{partcile}$ (i.e., lower κ^{-1}).

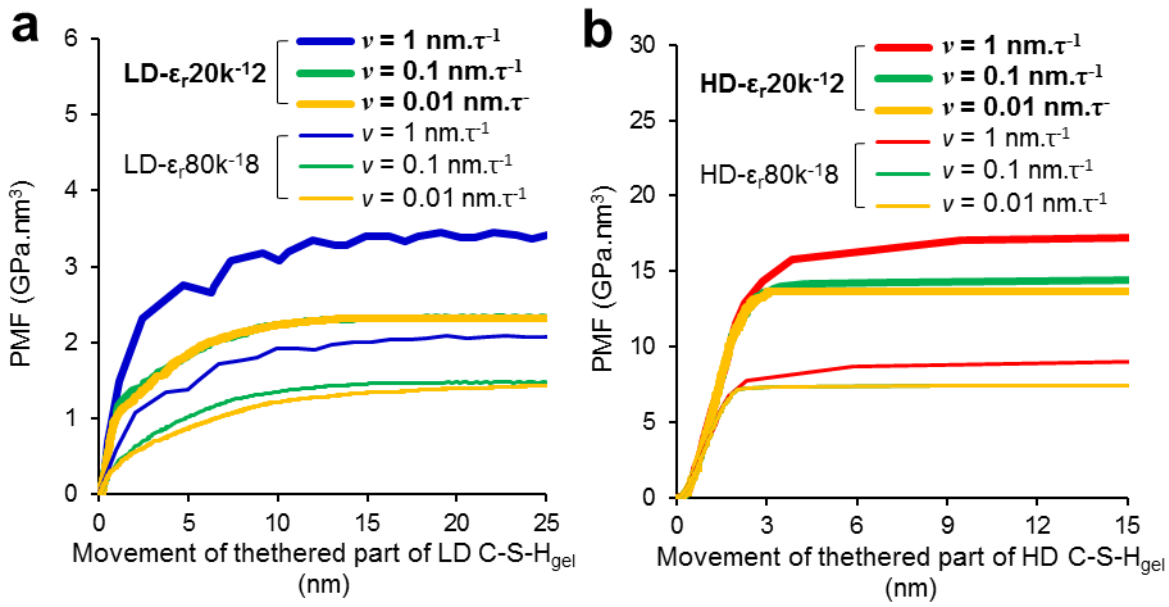

Figure 17. Profile of potential mean force (PMF) of (a) LD C-S-H_{gel} and (b) HD C-S-H_{gel} from steered molecular dynamics (SMD) with varied pulling speed between 1 nm.τ^{-1} and 0.01 nm.τ^{-1}. The PMF is normalized to the value per 1 nm^2.

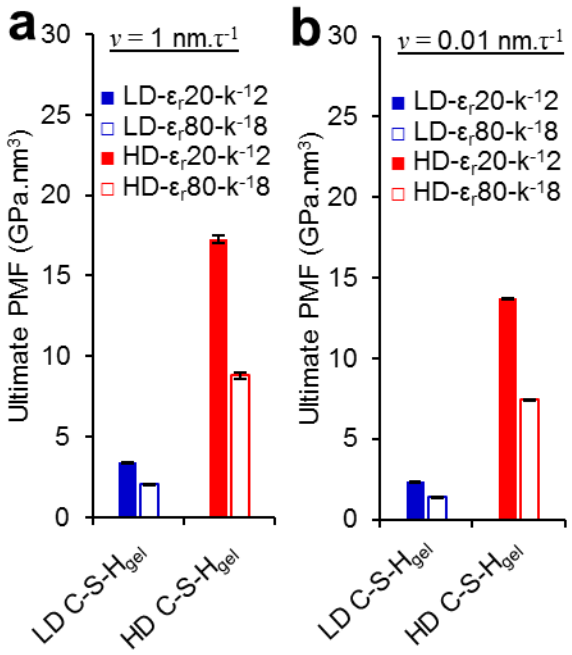

Figure 18. Ultimate PMF with pulling speeds of (a) 1 nm.τ^{-1} and (b) 0.01 nm.τ^{-1}.

4. Conclusion

In this study, the effects of the ionic characteristics of the gel-pore solution of HCP – *as represented by the dielectric constant (ε_r) and Debye length (κ^{-1})* – on the packing density (η) and compressive properties (i.e., Young's modulus E_c, hardness H_c, and strength $f_{c\text{-}u}$) of LD and HD C-S-H_{gel}, the main products of cement hydration, were investigated using mesoscale simulations of monodispersed and polydispersed spherical C-S-$H_{particle}$ systems. Overall, the simulated results of η, E_c, and H_c of LD and HD C-S-H_{gel} agreed well with the experimental data reported in the literature for HCP. The simulation results showed that changes in ε_r and κ^{-1} values influenced the inter-C-S-$H_{particle}$ distance of C-S-H_{gel} and resulted in changes in η and cohesion, which consequently influenced the E_c, H_c, and $f_{c\text{-}u}$ of the C-S-H_{gel}. The lower ε_r and κ^{-1} values, which were characteristics of a higher ionic concentration of the gel-pore solution, resulted in a greater packing density and, in turn, an overall greater stiffness, hardness, and strength of the C-S-H_{gel}. This trend was consistent with the higher nanoindentation modulus of C-S-H_{gel} reported in the literature in the presence of salts. The results of this study provided insight into the mechanisms by which the gel-pore ionic solution affects the mechanical properties of C-S-H_{gel} and showed that

ε_r and κ^{-1} could be useful parameters for engineering cementitious materials with ionic substances such as salt based chemical-admixture, seawater, and sea sand.

Acknowledgements

The authors would like to acknowledge the financial support of the Hong Kong Research Grants Council Theme Based Research Scheme.

References

[1] S. Pyo, M. Tafesse, H. Kim, H.-K. Kim, Effect of chloride content on mechanical properties of ultra high performance concrete, Cement and Concrete Composites, 84 (2017) 175-187.

[2] M. Jebli, F. Jamin, C. Pelissou, E. Malachanne, E. Garcia-Diaz, M.S. El Youssoufi, Leaching effect on mechanical properties of cement-aggregate interface, Cement and Concrete Composites, 87 (2018) 10-19.

[3] Y. Yang, R.A. Patel, S.V. Churakov, N.I. Prasianakis, G. Kosakowski, M. Wang, Multiscale modeling of ion diffusion in cement paste: electrical double layer effects, Cement and Concrete Composites, 96 (2019) 55-65.

[4] D. Lau, W. Jian, Z. Yu, D. Hui, Nano-engineering of construction materials using molecular dynamics simulations: Prospects and challenges, Composites Part B: Engineering, 143 (2018) 282-291.

[5] Y.L. Yaphary, R.H. Lam, D. Lau, Reduction in cement content of normal strength concrete with used engine oil (UEO) as chemical admixture, Construction and Building Materials, 261 (2020) 119967.

[6] P. Juilland, L. Nicoleau, R.S. Arvidson, E. Gallucci, Advances in dissolution understanding and their implications for cement hydration, RILEM Technical Letters, 2 (2017) 90-98.

[7] J.J. Chen, J.J. Thomas, H.F. Taylor, H.M. Jennings, Solubility and structure of calcium silicate hydrate, Cement and concrete research, 34 (2004) 1499-1519.

[8] J.J. Thomas, H.M. Jennings, A colloidal interpretation of chemical aging of the CSH gel and its effects on the properties of cement paste, Cement and concrete research, 36 (2006) 30-38.

[9] T.C. Powers, T.L. Brownyard, Studies of the physical properties of hardened Portland cement paste, Journal Proceedings1946, pp. 101-132.
[10] T. Petersen, P.-L. Valdenaire, R. Pellenq, F.-J. Ulm, A reaction model for cement solidification: Evolving the C–S–H packing density at the micrometer-scale, Journal of the Mechanics and Physics of Solids, 118 (2018) 58-73.
[11] H.M. Jennings, A model for the microstructure of calcium silicate hydrate in cement paste, Cement and concrete research, 30 (2000) 101-116.
[12] P.D. Tennis, H.M. Jennings, A model for two types of calcium silicate hydrate in the microstructure of Portland cement pastes, Cement and concrete research, 30 (2000) 855-863.
[13] G. Constantinides, F.-J. Ulm, The effect of two types of CSH on the elasticity of cement-based materials: Results from nanoindentation and micromechanical modeling, Cement and concrete research, 34 (2004) 67-80.
[14] R.J.-M. Pellenq, A. Kushima, R. Shahsavari, K.J. Van Vliet, M.J. Buehler, S. Yip, F.-J. Ulm, A realistic molecular model of cement hydrates, Proceedings of the National Academy of Sciences, 106 (2009) 16102-16107.
[15] A.J. Allen, J.J. Thomas, H.M. Jennings, Composition and density of nanoscale calcium–silicate–hydrate in cement, Nature materials, 6 (2007) 311.
[16] F.J. Ulm, M. Vandamme, C. Bobko, J. Alberto Ortega, K. Tai, C. Ortiz, Statistical indentation techniques for hydrated nanocomposites: concrete, bone, and shale, Journal of the American Ceramic Society, 90 (2007) 2677-2692.
[17] W.-S. Chiang, E. Fratini, P. Baglioni, D. Liu, S.-H. Chen, Microstructure determination of calcium-silicate-hydrate globules by small-angle neutron scattering, The Journal of Physical Chemistry C, 116 (2012) 5055-5061.
[18] S. Masoumi, S. Zare, H. Valipour, M.J. Abdolhosseini Qomi, Effective Interactions Between Calcium-Silicate-Hydrate Nanolayers, The Journal of Physical Chemistry C, 123 (2019) 4755-4766.
[19] O. Mendoza, C. Giraldo, S.S. Camargo Jr, J.I. Tobón, Structural and nano-mechanical properties of Calcium Silicate Hydrate (CSH) formed from alite hydration in the presence of sodium and potassium hydroxide, Cement and Concrete Research, 74 (2015) 88-94.

[20] J. Wang, E. Liu, L. Li, Multiscale investigations on hydration mechanisms in seawater OPC paste, Construction and Building Materials, 191 (2018) 891-903.
[21] C. Plassard, E. Lesniewska, I. Pochard, A. Nonat, Nanoscale experimental investigation of particle interactions at the origin of the cohesion of cement, Langmuir, 21 (2005) 7263-7270.
[22] K. Ioannidou, R.J.-M. Pellenq, E. Del Gado, Controlling local packing and growth in calcium–silicate–hydrate gels, Soft Matter, 10 (2014) 1121-1133.
[23] M.E. Leunissen, C.G. Christova, A.-P. Hynninen, C.P. Royall, A.I. Campbell, A. Imhof, M. Dijkstra, R. Van Roij, A. Van Blaaderen, Ionic colloidal crystals of oppositely charged particles, Nature, 437 (2005) 235.
[24] J.W. Bullard, H.M. Jennings, R.A. Livingston, A. Nonat, G.W. Scherer, J.S. Schweitzer, K.L. Scrivener, J.J. Thomas, Mechanisms of cement hydration, Cement and concrete research, 41 (2011) 1208-1223.
[25] A. Nonat, The structure and stoichiometry of CSH, Cement and Concrete Research, 34 (2004) 1521-1528.
[26] S. Garrault, E. Finot, E. Lesniewska, A. Nonat, Study of CSH growth on C 3 S surface during its early hydration, Materials and structures, 38 (2005) 435-442.
[27] H. Liu, S. Dong, L. Tang, N.A. Krishnan, E. Masoero, G. Sant, M. Bauchy, Long-term creep deformations in colloidal calcium–silicate–hydrate gels by accelerated aging simulations, Journal of colloid and interface science, 542 (2019) 339-346.
[28] H. Liu, S. Dong, L. Tang, N.A. Krishnan, G. Sant, M. Bauchy, Effects of polydispersity and disorder on the mechanical properties of hydrated silicate gels, Journal of the Mechanics and Physics of Solids, 122 (2019) 555-565.
[29] H. Liu, T. Du, N.A. Krishnan, H. Li, M. Bauchy, Topological optimization of cementitious binders: advances and challenges, Cement and Concrete Composites, 101 (2019) 5-14.
[30] L. Skinner, S. Chae, C. Benmore, H. Wenk, P. Monteiro, Nanostructure of calcium silicate hydrates in cements, Physical review letters, 104 (2010) 195502.
[31] E. Masoero, E. Del Gado, R.-M. Pellenq, F.-J. Ulm, S. Yip, Nanostructure and nanomechanics of cement: polydisperse colloidal packing, Physical review letters, 109 (2012) 155503.

[32] S.D. Palkovic, S. Yip, O. Büyüköztürk, A cohesive-frictional force field (CFFF) for colloidal calcium-silicate-hydrates, Journal of the Mechanics and Physics of Solids, 109 (2017) 160-177.
[33] H. Liu, L. Tang, N.A. Krishnan, G. Sant, M. Bauchy, Structural percolation controls the precipitation kinetics of colloidal calcium–silicate–hydrate gels, Journal of Physics D: Applied Physics, 52 (2019) 315301.
[34] I. Pointeau, P. Reiller, N. Macé, C. Landesman, N. Coreau, Measurement and modeling of the surface potential evolution of hydrated cement pastes as a function of degradation, Journal of colloid and interface science, 300 (2006) 33-44.
[35] L. Nachbaur, P.-C. Nkinamubanzi, A. Nonat, J.-C. Mutin, Electrokinetic properties which control the coagulation of silicate cement suspensions during early age hydration, Journal of Colloid and Interface Science, 202 (1998) 261-268.
[36] B. Jönsson, H. Wennerström, A. Nonat, B. Cabane, Onset of cohesion in cement paste, Langmuir, 20 (2004) 6702-6709.
[37] D. Lowke, C. Gehlen, The zeta potential of cement and additions in cementitious suspensions with high solid fraction, Cement and Concrete Research, 95 (2017) 195-204.
[38] A.-P. Hynninen, M. Dijkstra, Phase diagrams of hard-core repulsive Yukawa particles, Physical Review E, 68 (2003) 021407.
[39] S. Safran, Statistical thermodynamics of surfaces, interfaces, and membranes, CRC Press2018.
[40] E. Masoero, E. Del Gado, R.J.-M. Pellenq, S. Yip, F.-J. Ulm, Nano-scale mechanics of colloidal C–S–H gels, Soft matter, 10 (2014) 491-499.
[41] H. Manzano, E. Masoero, I. Lopez-Arbeloa, H.M. Jennings, Shear deformations in calcium silicate hydrates, Soft Matter, 9 (2013) 7333-7341.
[42] A. Poursaee, C. Hansson, Reinforcing steel passivation in mortar and pore solution, Cement and Concrete Research, 37 (2007) 1127-1133.
[43] Y. Elakneswaran, T. Nawa, K. Kurumisawa, Electrokinetic potential of hydrated cement in relation to adsorption of chlorides, Cement and Concrete Research, 39 (2009) 340-344.
[44] C.Y. Chan, R.J. Knight, Determining water content and saturation from dielectric measurements in layered materials, Water Resources Research, 35 (1999) 85-93.

560 [45] S. Plimpton, Fast parallel algorithms for short-range molecular dynamics, Journal of
561 computational physics, 117 (1995) 1-19.
562 [46] D. Hou, H. Ma, Y. Zhu, Z. Li, Calcium silicate hydrate from dry to saturated state: structure,
563 dynamics and mechanical properties, Acta materialia, 67 (2014) 81-94.
564 [47] Y.L. Yaphary, D. Lau, F. Sanchez, C.S. Poon, Effects of sodium/calcium cation exchange
565 on the mechanical properties of calcium silicate hydrate (CSH), Construction and Building
566 Materials, 243 (2020) 118283.
567 [48] M. Abdolhosseini Qomi, D. Ebrahimi, M. Bauchy, R. Pellenq, F.-J. Ulm, Methodology for
568 estimation of nanoscale hardness via atomistic simulations, Journal of Nanomechanics and
569 Micromechanics, 7 (2017) 04017011.
570 [49] M.A. Qomi, K. Krakowiak, M. Bauchy, K. Stewart, R. Shahsavari, D. Jagannathan, D.B.
571 Brommer, A. Baronnet, M.J. Buehler, S. Yip, Combinatorial molecular optimization of
572 cement hydrates, Nature communications, 5 (2014) 4960.
573 [50] M. Bauchy, M.J.A. Qomi, C. Bichara, F.-J. Ulm, R.J.-M. Pellenq, Rigidity transition in
574 materials: hardness is driven by weak atomic constraints, Physical review letters, 114
575 (2015) 125502.
576 [51] B. Isralewitz, M. Gao, K. Schulten, Reconstructing potential energy functions from
577 simulated force-induced unbinding processes, Curr. Opin. Struct. Biol, 11 (2001) 224-230.
578 [52] S. Park, K. Schulten, Calculating potentials of mean force from steered molecular dynamics
579 simulations, The Journal of chemical physics, 120 (2004) 5946-5961.
580 [53] V. Živica, Effects of the very low water/cement ratio, Construction and building materials,
581 23 (2009) 3579-3582.
582 [54] M. Juenger, P. Monteiro, E. Gartner, G. Denbeaux, A soft X-ray microscope investigation
583 into the effects of calcium chloride on tricalcium silicate hydration, Cement and Concrete
584 Research, 35 (2005) 19-25.
585 [55] Y. Elakneswaran, T. Nawa, K. Kurumisawa, Zeta potential study of paste blends with slag,
586 Cement and Concrete Composites, 31 (2009) 72-76.
587 [56] S. Lesko, E. Lesniewska, A. Nonat, J.-C. Mutin, J.-P. Goudonnet, Investigation by atomic
588 force microscopy of forces at the origin of cement cohesion, Ultramicroscopy, 86 (2001)
589 11-21.

590 [57] Z. Yu, A. Zhou, D. Lau, Mesoscopic packing of disk-like building blocks in calcium silicate
591 hydrate, Scientific reports, 6 (2016) 36967.
592 [58] J. Hasted, D. Ritson, C. Collie, Dielectric properties of aqueous ionic solutions. Parts I and
593 II, The Journal of Chemical Physics, 16 (1948) 1-21.
594 [59] W.R. Fawcett, A.C. Tikanen, Role of solvent permittivity in estimation of electrolyte
595 activity coefficients on the basis of the mean spherical approximation, The Journal of
596 Physical Chemistry, 100 (1996) 4251-4255.
597